CrystEngComm

PAPER

Check for updates

Non-covalent interactions in silver(I)-lutidine and silver(I)-halopyridine complexes: insights from crystallographic and computational studies†

Enzo La Gorcé, [iD] Tristan K. Theunissen and Susan A. Bourne [iD] *

Discrete silver(I) coordination complexes with pyridyl derivatives were investigated to determine the prominent non-covalent interactions (NCIs) that stabilize the complexes. Four dimethylpyridines (or lutidines) were used to prepare [Ag(2,3-Lut)$_2$(NO$_3$)] (**I**), [Ag(2,6-Lut)$_2$(NO$_3$)] (**II**), [Ag(3,4-Lut)$_2$(NO$_3$)(H$_2$O)] (**III**), and [Ag(3,5-Lut)$_3$(NO$_3$)] (**IV**). Another series of complexes were prepared from 3-chloropyridine and 3-bromopyridine: [Ag(3-Clpy)$_3$NO$_3$] (**V**), [Ag(3-Brpy)$_3$(NO$_3$)] (**VI**) and [Ag(3-Brpy)$_2$(NO$_3$)] (**VII**). Spectroscopic and structural studies revealed a range of NCIs in each structure, including hydrogen bonding, halogen bonding, Ag···H agostic interactions, and Ag···π and π···π interactions. The AgL$_2$ complexes adopted an almost linear coordination geometry, except for **VII**, which exhibited a bent geometry. The AgL$_3$ complexes adopted a propeller conformation and were packed in a tail-and-groove arrangement. Computational studies were used to confirm the metal–ligand charge transfer (MLCT) characteristics of the electronic transitions observed in the UV spectra. A potential energy surface scan of compound **I** revealed two distinct conformations with a low rotational energy barrier.

Introduction

The use of low oxidation state metal compounds is becoming a fundamental part in modern-day chemistry. Silver(I) complexes have long been known to have medicinal and other useful physical properties, which have led to a great deal of interest in characterising a wide range of coordination compounds.

In addition to antibacterial properties,[1] silver compounds have shown promise in cancer therapy due to their ability to balance low toxicity with high efficacy against cancer cells, whereas other metal-based drugs—such as those containing platinum, gold, or copper—demonstrate potent anticancer activity but at the cost of harmful side effects.[2] Silver(I) complexes have demonstrated the potential to minimize these drawbacks, with recent studies showing their capability to outperform cisplatin in terms of cytotoxic activity.[3,4] Silver(I)-based coordination polymers (CPs) have shown promise as anticancer agents due to their strong binding affinity to DNA in cancer cells, leading to DNA cleavage and cell apoptosis. For example, Feng *et al.* synthesized an Ag-based CP that demonstrated high potency against HeLa and

MCF-7 cells, with cytotoxicity comparable to those of established agents like 5-fluorouracil and cisplatin. Fluorescence studies indicated a higher binding affinity of this CP to DNA, as evidenced by photoluminescence quenching.[5]

Given the interest in silver(I) coordination compounds, a comprehensive understanding of the interactions between silver(I) ions and the building units of these frameworks is essential. Silver(I) has a d^{10} electron configuration, which allows for potential luminescent activity if coordinated to a ligand with an empty π*-orbital that aligns with the filled d-orbital, making it feasible for photochemistry and sensing applications.[6,7] As a soft Lewis acid, silver can adopt a range of coordination geometries, which allows for the adoption of diverse coordination numbers and the formation of various inorganic building units with flexible geometries.[8–10]

Non-covalent interactions (NCIs) play a significant role in chemistry, contributing to the structural integrity and functionality of many biological and synthetic systems. For instance, the three-dimensional (3-D) structure of DNA is maintained through several NCIs, such as π–π stacking and hydrogen bonding, which stabilize the interactions between both its building blocks and the surrounding environment, directing and guiding its overall structure.[11] Unlike traditional covalent or ionic bonds, where electrons are shared or donated between atoms, NCIs involve long-range interactions between different molecules (intermolecular) or within different parts of the same molecule

Centre for Supramolecular Chemistry Research, Department of Chemistry, University of Cape Town, Private Bag X3, Rondebosch 7701, South Africa. E-mail: susan.bourne@uct.ac.za

(intramolecular).[12] NCIs come in various forms, including hydrogen bonding, halogen bonding, hydrophobic interaction, electrostatic forces, and π–π stacking, often involving a combination of multiple interactions in a system.[13–15]

Previous studies by some of us aimed to better understand silver(I) pyridyl complexes and their NCIs, focusing on the silver metal centre in these interactions.[16] In this investigation, halogens were employed to strengthen NCIs through uncommon semi-coordination bonds (sXBs). Grouping pyridyl ligands, such as halogenated pyridyls, picolines, and lutidines, allowed for a detailed analysis of how varying the substituents and their positions on the nitroaromatic ring affected these interactions. In that study, the $[Ag_2(OBn)_2]$ (where OBn is benzoate) core was coordinated to the ligands 3-chloropyridine, 2-bromopyridine, 2-iodopyridine, and 2-picoline. Fig. 1 shows the $[Ag_2(OBn)_2]$ core structure and those of the silver(I)-halopyridyl compounds.

In this study, discrete silver(I) coordination complexes were used to investigate the prominent non-covalent interactions (NCIs) present within the crystal structures. By employing commonly used pyridyl ligands, the aim was to establish foundational principles that could guide the design of coordination compounds or metal–organic frameworks (MOFs) in future research. Here, we report silver(I) coordination compounds with two series of ligands (Fig. S1). First, the dimethylpyridines (or lutidines) were used to prepare $[Ag(2,3\text{-Lut})_2(NO_3)]$ (**I**), $[Ag(2,6\text{-Lut})_2(NO_3)]$ (**II**), $[Ag(3,4\text{-Lut})_2(NO_3)(H_2O)]$ (**III**), and $[Ag(3,5\text{-Lut})_3(NO_3)]$ (**IV**). Then, we used 3-chloropyridine and 3-bromopyridine to prepare a series $[Ag(3\text{-Clpy})_3NO_3]$ (**V**), $[Ag(3\text{-Brpy})_3(NO_3)]$ (**VI**) and $[Ag(3\text{-Brpy})_2(NO_3)]$ (**VII**). Spectroscopic and structural studies

revealed a number of NCIs present in each, and computational studies were used to quantify these further.

Experimental

Materials and instrumentation

All reagents and solvents were purchased from Merck and Sigma-Aldrich ($\geq$99% purity). Fourier-transform infrared (FT-IR) spectra were recorded on Perkin Elmer UATR Two (4000–400 cm^{-1}). Emission spectra were obtained using a Cary Varian Eclipse Fluorescence spectrophotometer at room temperature, with a scanning range of 270–600 nm. Ultraviolet visible (UV-vis) spectra were measured using a Cary 60 UV-vis spectrophotometer with a 200–800 nm scan and a xenon flash lamp (80 Hz). Powder X-ray diffraction (PXRD) patterns were recorded using a Bruker D8 PXRD diffractometer with Cu Kα radiation scanned over the 2θ range of 4–40°.

Synthesis of silver(I)-lutidine complexes (I–IV)

1.00 mL (1 mmol) of a silver nitrate (AgNO$_3$) solution was mixed with the appropriate volume of the relevant lutidine ligands based on the desired ratios, and 1.00 mL of a 0.25 mol dm^{-3} solution of sodium benzoate (NaOBn) was added to each vial. For the 1:1:1 ratio, the following volumes of lutidine were added to their respective vials: 113 μL of 2,3-Lut, 116 μL of 2,6-Lut, 112 μL of 3,4-Lut, and 114 μL of 3,5-Lut. The mixtures were then stirred for 15–20 minutes, with 1–4 mL of acetonitrile gradually added to each vial until a clear solution was obtained. Once fully dissolved, the vials were covered in aluminium foil and stored in a dark space, allowing for crystallisation, with **I**, **II**, **III** and **IV** crystallizing
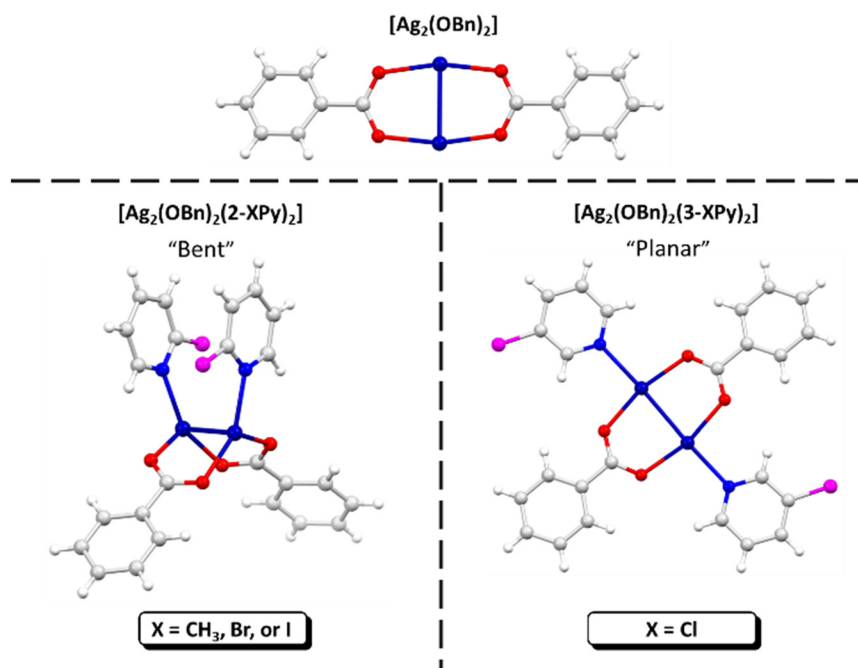

Fig. 1 Core structures of (top) $[Ag_2(OBn)_2]$ and (bottom) silver(I)-halopyridyl compounds.

after several days. Since no benzoate was included in the compounds, we repeated the synthesis using a 2:1 ratio of lutidine:metal. 1.00 mL (1 mmol) of AgNO$_3$ solution was added to volumes of 227 μL, 233 μL, 225 μL and 228 μL of the respective lutidines. The mixtures were stirred for 15–20 minutes, and 1–4 mL of acetonitrile was gradually added to each vial until a clear solution was obtained. Once fully dissolved, the vials were covered in aluminium foil and stored in a dark space, allowing for crystallisation. The same compounds were crystallized using this method. FT-IR (DMSO, cm^{-1}): **I** – 3081 (w), 1594 (w), 1442 (m), 1321 (s), 1189 (m), 1131 (m), 789 (m), 718 (m). **II** – 2917 (w), 2335 (w), 1579 (m), 1469 (m), 1314 (s), 1160 (m), 1040 (m), 789 (s). **III** – 2973 (w), 1612 (m), 1442(m), 1315 (s), 1203 (m), 1083 (m), 826 (s), 721 (w). **IV** – 2923 (w), 1598 (w), 1456 (w), 1313 (s), 1241 (s), 1147 (m), 870 (m), 708 (s). UV-vis (DMSO, nm): **I** – 265. **II** – 267. **III** – 264. **IV** – 271. Emission (DMSO, nm): **I** – 361. **II** – 374. **III** – 360. **IV** – 359.

Synthesis of silver(I)-halogenated pyridyl complexes (V–VII)

A 2:1 ratio of ligand:metal was used initially. 2 mmol of 3-chloropyridine (3-Clpy, 190 μL) or 3-bromopyridine (3-Brpy, 193 μL) was added to 1.00 mL of silver nitrate (AgNO$_3$) solution (1 mmol), followed by the addition of acetonitrile in minimal amounts until a clear solution was obtained. The solution was stirred for 15 minutes, covered in aluminium foil and left to crystallise, forming compounds **V** and **VI**. The synthesis was repeated using a 4:1 ratio of ligand:metal, *viz.* 380 μL (4 mmol) of 3-Clpy or 385 μL (4 mmol) of 3-Brpy was added to 1 mmol of AgNO$_3$. The solution was stirred for 15 minutes, covered in aluminium foil and left to crystallise, forming compounds **V** and **VII**. FT-IR (DMSO, cm-1): **V** – 3058 (w), 1583 (w), 1469 (m), 1349 (s), 1194 (w), 796 (s). **VI** – 3087 (w), 1584 (w), 1423 (m), 1301 (s), 694 (s). **VII** – 3055 (w), 1582 (w), 1466 (m), 1345 (s), 693 (m). UV-vis (DMSO, nm): **V** – 268. **VI** – 268. **VII** – 270. Fluorescence (DMSO, nm): **V** – 363. **VI** – 362. **VII** – 359.

X-ray structure determination

Single crystal X-ray diffraction (SCXRD) data were collected at 173(2) K using a Bruker Kappa Apex DUO II diffractometer with monochromated Mo Kα radiation. APEX II software was used to control the data selection and unit cell determination; the intensity data were reduced using SAINT-Plus[17] with the ω scan technique. Absorption corrections were performed using SADABS.[18] XPREP[19] was used to prepare the input files for SHELXT. OLEX2 (ref. 20) was used as a graphical interface for the crystal structure solution and refinement, which was performed using the SHELX[21] suite of programs. Non-hydrogen atoms were refined anisotropically before adding the hydrogen atoms, which were refined using a riding model with isotropic thermal parameters linked to their parent atoms. Mercury[22] was used to generate diagrams and analyse close contacts. Crystallographic parameters are given in Tables S1 and S2.

Computational methodology

Density functional theory (DFT) computations were performed on the Ag(I) complexes using the *Gaussian 16* software package.[23] Geometry optimisations and time-dependent density-functional theory (TDDFT) calculations of [Ag(3-Brpy)$_3$(NO$_3$)] and [Ag(2,3-Lut)$_2$(NO$_3$)] (compounds **I** and **VI**) were carried out using the B3LYP functional,[24,25] in conjunction with the cc-pVDZ[26] basis set for all atoms except silver, for which the cc-pDVZ-PP pseudopotential[27] was employed. Grimme's D3 empirical dispersion correction was applied to account for long-range interactions.[28,29] Input coordinates for the complexes were generated using *Chemcraft*.[30] The nature and energies of the Kohn–Sham molecular orbitals (MOs) were obtained from the DFT output files and visualized using *Chemcraft* for analysis. A relaxed potential energy surface (PES) scan was performed on compound **I** at the B3LYP/gen level of the theory. The dihedral rotation of the pyridyl ring was explored in thirty steps of 10° increments, spanning 0–240°. Hirshfeld surface (HS) analysis was performed using the *CrystalExplorer 17* program package.[31]

Results and discussion

Crystallographic analysis was performed on two groups of complexes, which were categorized by the ligands used: lutidines and halogenated pyridines. This analysis includes single crystal X-ray diffraction (SCXRD), powder X-ray diffraction (PXRD), and Hirshfeld surface analysis, where applicable. Computational studies were conducted on selected compounds to further understand the nature of the NCIs present.

Structural analyses of [Ag(2,3-Lut)$_2$(NO$_3$)] (I), [Ag(2,6-Lut)$_2$NO$_3$] (II) and [Ag(3,4-Lut)$_2$(NO$_3$)(H$_2$O)] (III)

Although not isostructural, these three compounds display the same coordination geometry and thus are discussed as a collective. **I** crystallizes in the orthorhombic space group *Pbcn*. The asymmetric unit (ASU) contains one silver(I) ion located on a 2-fold rotation axis, one 2,3-lutidine (2,3-Lut) ligand, and a nitrate (NO$_3^-$) counterion (Fig. 2). The complete molecule is symmetry-generated by the operator 1 − x, y, 1/2 − z, resulting in a two-coordinate, near-linear coordination geometry.

II and **III** crystallize in space groups *P2$_1$/n* and *P$_c$*, respectively, and their ASUs consist of a silver(I) ion, two lutidine ligands and a nitrate counterion. **III** also includes a guest water molecule (Fig. 2).

All three structures have a linear coordination geometry at the silver ion with N–Ag–N bond angles of 173.16(6)°, 170.72(9)° and 170.0(4)° for **I**, **II** and **III**, respectively (Tables S3a–c). Their silver–nitrogen bond distances are 2.15(12), 2.18(3) and 2.14(6) Å, respectively (Tables S3a–c).

The packing arrangement in **I** consists of three alternating layers (Fig. 3a and b). Each lutidine methyl group forms weak
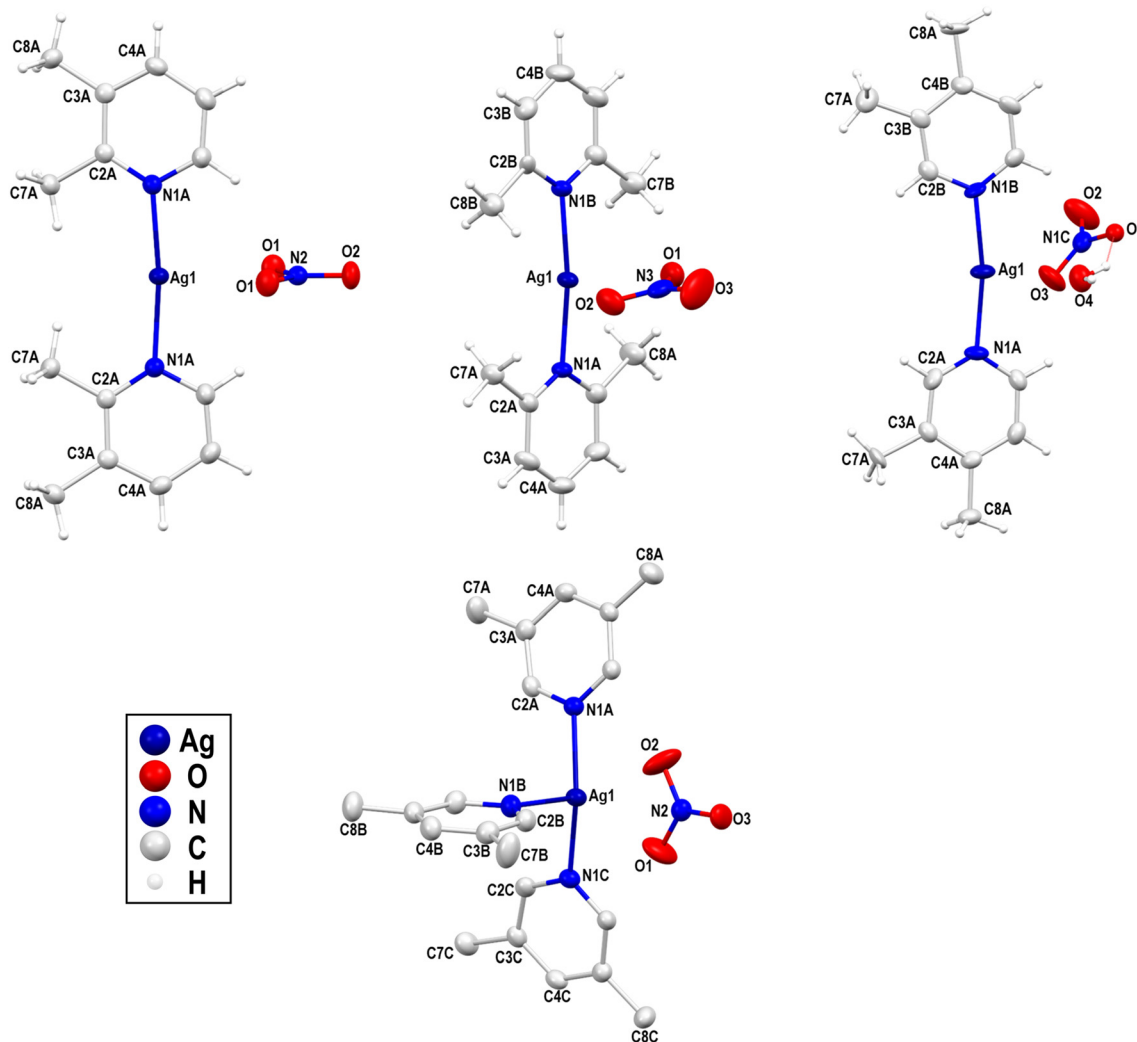
Fig. 2 Asymmetric units in the crystal structures of **I–IV** showing the atom numbering schemes. All displacement ellipsoids are drawn at 50% probability. The complete molecule of **I** is generated by the symmetry operator $1 - x, y, \frac{1}{2} - z$.

C–H···O hydrogen bonds with two nitrate ions, forming diamond-shaped short contacts (Fig. 3c). Weak hydrogen bonds are also observed involving the aromatic hydrogens, forming a network of interactions that further stabilise the packing arrangement (Fig. S2 and S3). Other notable interactions that reinforce the packing of **I** are the silver–

Fig. 3 (a) Packing in **I** viewed along the *c*-axis and (b) molecules arranged in alternating layers. Hydrogen atoms are omitted for clarity. (c) Weak hydrogen bonding in **I**.
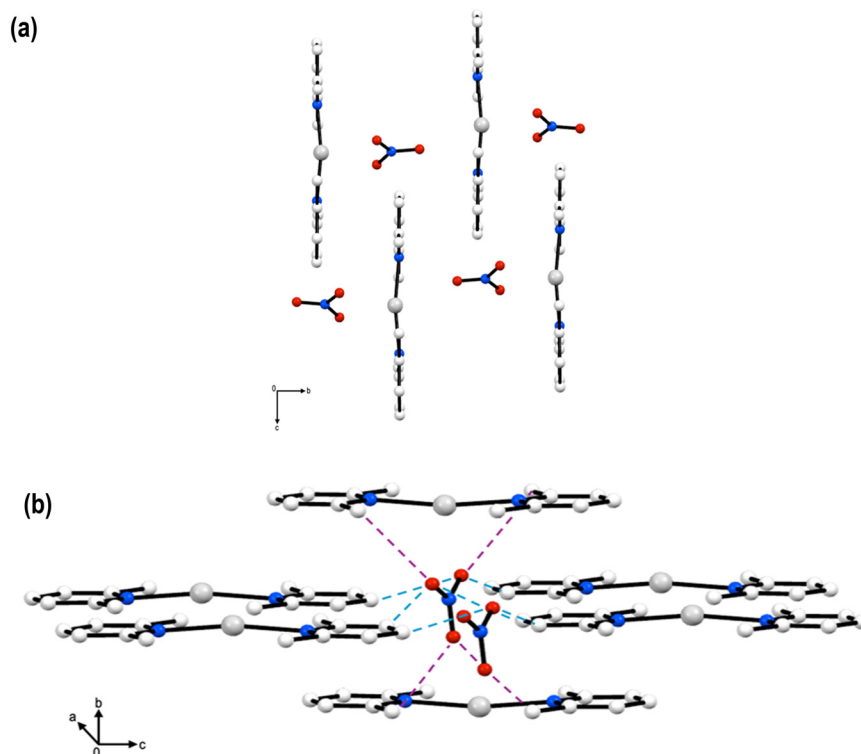
Fig. 4 (a) Packing in **II** showing a layered structure. (b) Simplified view of interactions in **II**; methyl hydrogen bonds in purple and aromatic hydrogen bonds in blue. Hydrogen atoms are omitted for clarity.

oxygen (nitrate) contact (Ag···O = 2.823(12) Å) and the silver–pyridyl π interaction (Ag···centroid = 3.609(1) Å).

Compound **II** packs in layers that are separated by nitrate molecules along all axes (Fig. 4a). These nitrate molecules facilitate packing through weak hydrogen bonding. Although there are no centroid–centroid interactions from the overlapping aromatic ring systems, the nitrate ions form weak C–H···O hydrogen bonds with both methyl and aromatic hydrogens. These are detailed in Table S3 and shown in Fig. 4b and S4. In **III**, layers of the silver complexes are interspersed among the nitrate and guest water molecules. The pyridyl rings centroid-to-centroid distances of 3.58(3) Å and 3.56(3) Å suggest the presence of weak π···π stacking (Fig. 5a). There are also silver–oxygen (water) interactions with a distance $d(H_2O···Ag)$ = 2.66(7) Å as well as interactions between the silver ion and oxygen from the

nitrate, $d(N–O···Ag)$ = 3.07(8) Å. Both distances are significantly lower than the sum of van der Waals radii for oxygen and silver ($R_O + R_{Ag}$ = 3.24 Å), indicating stabilising effects from orbital interactions. This is illustrated in Fig. 5b and S5, showing the zig-zag O···Ag interactions.

The experimental powder X-ray diffraction patterns (SI) closely match the calculated patterns for **I–III**, with all major peaks from the calculated pattern present in the experimental data, indicating bulk purity for the complexes.

Structural analysis of [Ag(3,5-Lut)₃(NO₃)] (IV)

The ASU for complex **IV** consists of one silver(I) ion, three 3,5-lutidine (3,5-Lut) ligands and a nitrate (NO₃⁻) counterion (Fig. 2), crystallizing in space group $P2_1/n$. The silver ion has a three-coordinate geometry in which the ligands adopt a
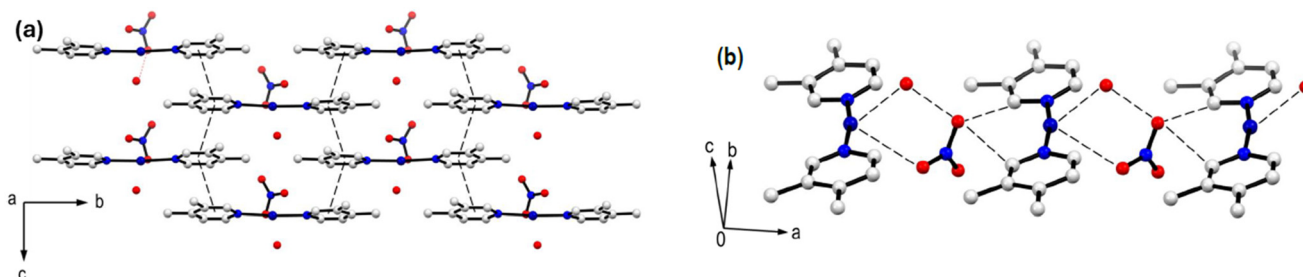

Fig. 5 (a) Packing in **III** with π···π interactions between the layers. (b) Silver–oxygen interactions in **III**. Hydrogen atoms are omitted for clarity.

propeller-like arrangement. This geometry facilitates crystal packing, with adjacent molecules aligning such that the "tail" of one propeller fits into the "groove" of a neighbouring molecule, Fig. 6. This difference in coordination geometry compared to the other lutidine ligands is possible because of the steric effects of the lutidine ligand, in which the methyl groups symmetrically face away from the coordinating nitrogen, allowing for more space around the silver(I) centre. The angles about the silver(I) ion deviated slightly from an ideal trigonal planar geometry as the 'propeller' forces the molecule out of planarity. The angles between the ligands are 105.29(7)° for ∠(N1A–Ag–N1B), 131.38(7)° for ∠(N1A–Ag–N1C), and 106.74(7)° for ∠(N1B–Ag–N1C). Further parameters are presented in Table S3d.

Fig. 6 also shows some of the NCIs in the packing of **IV**. Each silver(I) ion is involved in an agostic interaction with methyl hydrogen on an adjacent molecule. The distance between the silver centres and the hydrogens $d(Ag\cdots H)$ is 2.89(2) Å, which is approximately equal to the sum of the van der Waals radii for silver and hydrogen, $(R_{Ag} + R_H) = 2.92$ Å, indicating molecular orbital interactions for these atoms. Fig. 6 shows how these agostic interactions (shown as black dashed lines) link adjacent molecules to form dimers. Hydrogen–π interactions ($d(H\cdots Cg) = 2.7(10)$–$2.94(10)$ Å) involving the other two lutidine arms on each molecule link these dimers in a staggered ladder arrangement (shown as light blue dashed lines in Fig. 6). These two interactions act simultaneously and reinforce each other by alternating along the b-axis.

Structural analyses of [Ag(3-Clpy)₃NO₃] (V), [Ag(3-Brpy)₃NO₃] (VI) and [Ag(3-Brpy)₂(NO₃)] (VII)

In order to expand the range of NCIs possible in this series of compounds, we used a similar process to prepare silver(I) complexes with the halogenated pyridines, 3-chloropyridine (3-Clpy) and 3-bromopyridine (3-Brpy). 3-Clpy formed [Ag(3-Clpy)₃NO₃] (**V**) from both the 2:1 and 4:1 reaction mixtures. Using a 2:1 reaction mixture with 3-Brpy resulted in the crystallization of [Ag(3-Brpy)₃NO₃] (**VI**), while a 4:1 reaction mixture gave [Ag(3-Brpy)₂(NO₃)] (**VII**). This result is counterintuitive but serves to illustrate the fine balance of energies in crystallization experiments. The three halogenated pyridine complexes described here are shown in Fig. 7 and 8, and further details are presented in Table S4. The experimental powder X-ray diffraction patterns (SI) closely match the calculated patterns for **V–VII**, confirming the bulk purity of the compounds.

The asymmetric units of **V** (Fig. S6) and **VI** (Fig. 7a) consist of one silver(I) ion, three X-py (Cl and Br, respectively) ligands and a nitrate anion. These compounds are isostructural, so only **VI** is described. Details for **V** are available in the SI material. The complexes have a three-coordinate geometry about the silver ion, where the ligands adopt a propeller-like arrangement. This geometry facilitates crystal packing, with adjacent molecules aligning such that the "tail" of one propeller fits into the "groove" of a neighbouring molecule, Fig. 7b. The angles between the silver ion and the pyridyl ligands for **VI** are 109.51(7)°, 132.44(5)° and 115.49(9)°, indicating a slight distortion from the ideal trigonal planar geometry.

The primary non-covalent interaction in the crystal structure of **VI** is π–π stacking between the aromatic pyridyl rings (i.e., π-systems) positioned one above the other. As depicted in Fig. 7b, distances between the centroids of pyridyl rings are indicated with red dashed lines. The centroid-to-centroid distance between rings Cg1 and Cg2 $d(Cg1\cdots Cg2)$ is 3.600(1) Å and that between Cg3 and Cg4, $d(Cg3\cdots Cg4)$ is 3.710(2) Å. These are suggestive of a weak
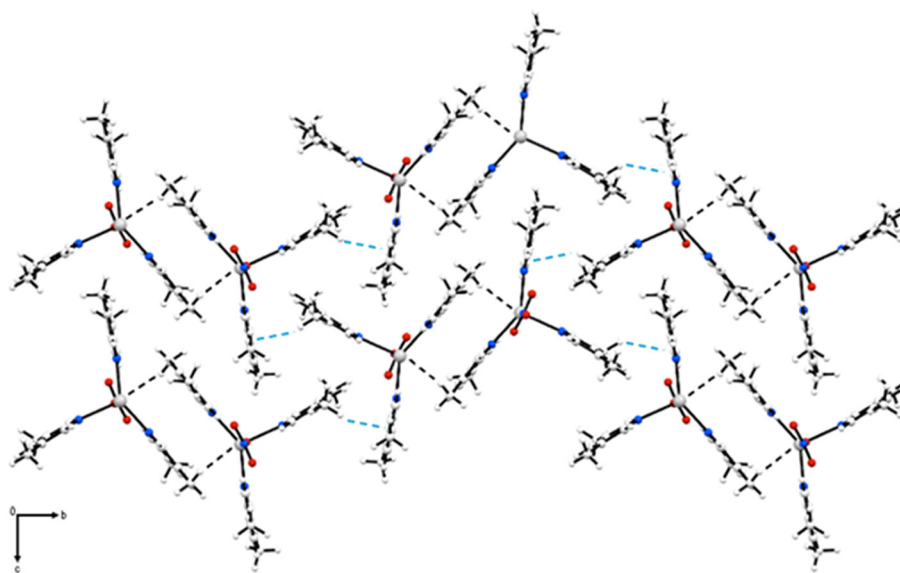

Fig. 6 Packing of complex **IV**, viewed down the a-axis, showing the 'tail and groove' packing of the molecules and illustrating the agostic (black) and hydrogen–centroid (light blue) interactions.
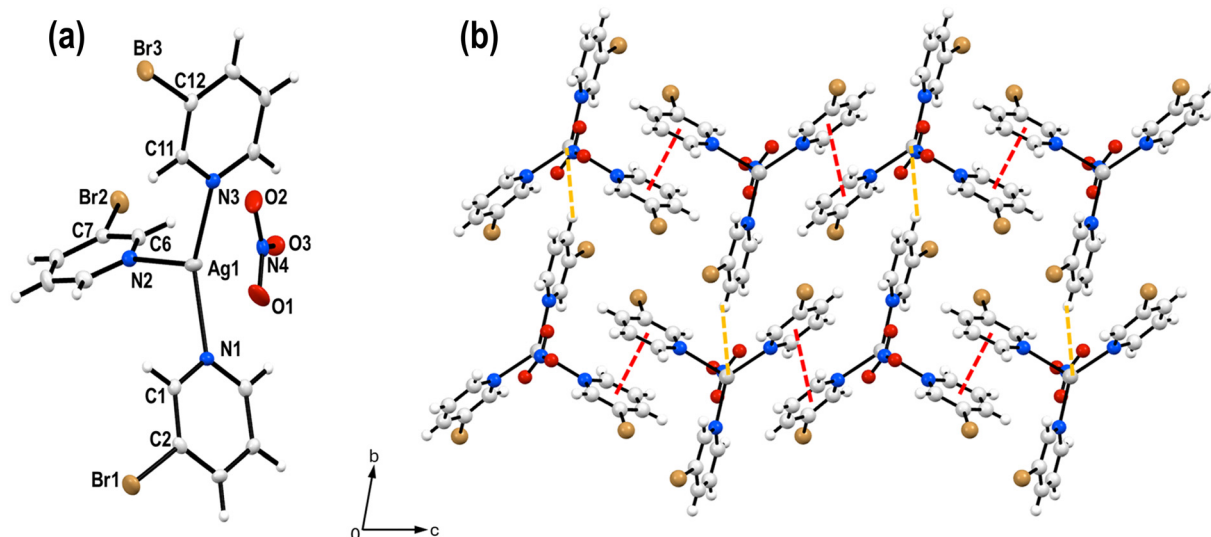
Fig. 7 (a) X-ray structure of ASU for complex **VI**, showing the Ag(ɪ) metal centre with three 3-Brpy ligands and an NO_3^- counterion. Thermal ellipsoids are drawn at 50% probability. (b) Packing arrangement of complex **VI** viewed along the *a*-axis, illustrating the π–π stacking interactions (red dashed lines) and hydrogen–silver (agostic) interactions (orange dashed lines). Hydrogen atoms are omitted for clarity.
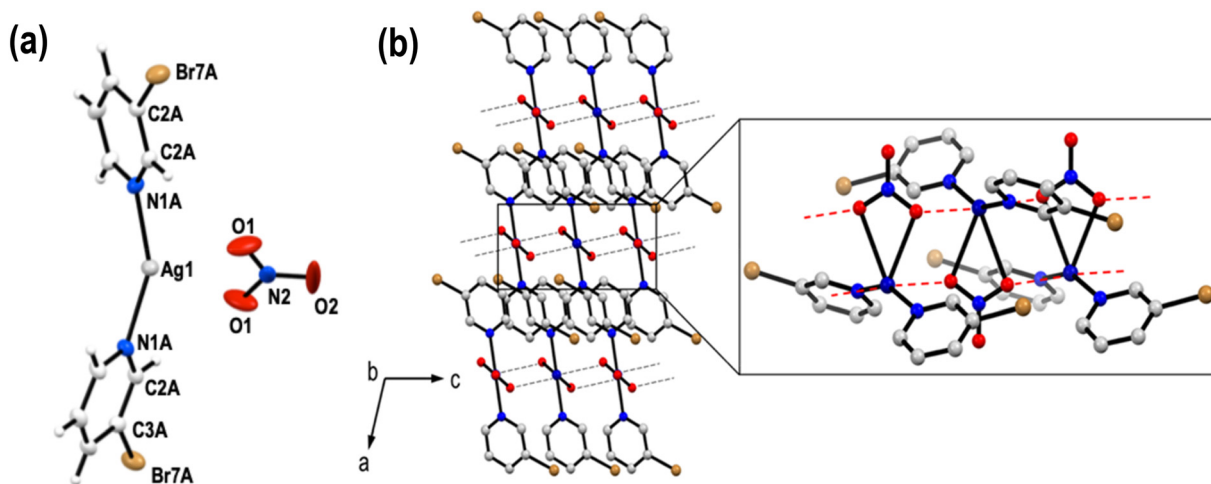

Fig. 8 (a) X-ray ASU of complex **VII**; symmetry-generated ligand labelled with (i) superscripts. *i* = 1 − *x*, *y*, 1/2 − *z*. Thermal ellipsoids are drawn at 50% probability. (b) Oxygen–silver interactions (black dashed lines) viewed along the *b*-axis. Packing is shown on the left side, with an enlarged and focused image on the right side, showing interactions with red dashed lines. Hydrogen atoms are omitted for clarity.

molecular orbital overlap between these rings. Hydrogen–silver agostic interactions have distances $d(Ag1\cdots H1(C2A))$ and $d(Ag2\cdots H2(C3A))$ of 3.009(4) Å, which is slightly longer than the sum of the van de Waals radii for Ag···H (2.92 Å). As mentioned earlier in the ASU description, the nitrate anion (NO_3) is responsible for the charge balance. Further analysis reveals that the NO_3 anion also influences packing. The silver(ɪ) metal centre is positively charged, whereas the nitrates are negatively charged, leading to a preferred alternating stacking of charges [$Ag^+\cdots O_2-N-O\cdots Ag^+$] (as illustrated in Fig. S7). The larger atomic radii of the halogens may lead to steric strain, which is alleviated by offset tail-and-groove packing in **V** and **VI**. There are bromine–bromine molecular interactions due to the closest Br–Br distance

being 3.773(4) Å, which is approximately equal to the sum of van de Waals radii for bromine, 3.7 Å. Like the agostic interactions, the halogen interaction acts as reinforcement towards overall crystal packing stability.

In **V**, a similar set of electrostatic interactions directs the packing (Fig. S8). The closest Cl-to-Cl distance is 3.793(9) Å, which is longer than the sum of the van der Waals radii for chlorine ($R_{Cl} + R_{Cl}$ = 3.5 Å), suggesting minimal direct interactions between chlorine atoms in this complex. In addition, hydrogen–silver (agostic) interactions are observed within the packing of complex **V**. The sum of van der Waals radii for Ag···H is ($R_{Ag} + R_H$ = 2.92 Å), which is comparable to the observed distance $d(Ag\cdots H)$ (2.987(4) Å). The nitrate ion is also involved in the packing of the complex through
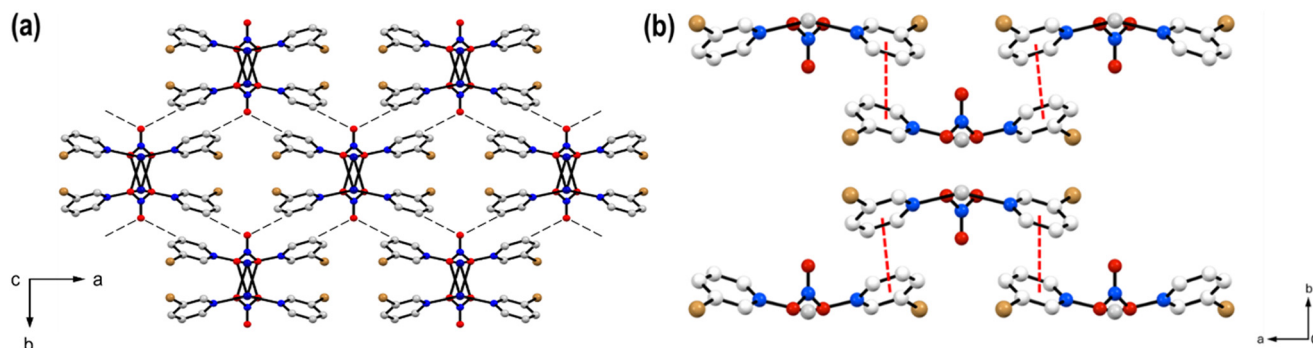
Fig. 9 (a) Hydrogen bonding paths present in complex **VII** viewed along the *c*-axis with interactions shown as dashed lines. Hydrogen atoms are omitted for clarity. (b) Illustration of weak π–π stacking interactions viewed down the *c*-axis, shown as red dashed lines. Hydrogen atoms are omitted for clarity.

interactions with the Ag$^+$ ion. This analysis of short contacts reveals that various NCIs can work cooperatively to influence crystal packing.

Similar to complex **I**, the asymmetric unit of **VII** consists of one silver(I) metal centre, one 3-bromopyridine (3-Brpy) ligand and a nitrate (NO$_3^-$) (Fig. 8a), with the second ligand being symmetry generated by the centre of inversion at $1 - x$, y, $1/2 - z$ in space group C2/c (Table S2). The ligands are equidistant from the metal centre with d(Ag1–N1A) = d(Ag1–N1A) = 2.211(3) Å, resulting in a two-coordinate complex. **VII** adopts a bent geometry in which ∠(N1A–Ag–N1A) = 153.17(13)°. Multiple interactions are present in complex **VII**: weak π–π stacking (from aromatic rings), hydrogen bonding between the pyridyl rings and nitrate molecules, silver–oxygen interaction from the nitrates and bromine–carbon interactions (Fig. 8b).

VII is influenced by a very weak π–π stacking interaction and various nitrate interactions. Analysing π–π stacking, overlapping centroids have a distance of 3.572(2) Å, Fig. 9b, indicating weak molecular orbital effects. This interaction minimally influences packing along the *b*-axis. The nitrate

molecules maintain a crucial role in the packing of **VII**, with involvement in both hydrogen bonding between oxygen and aromatic hydrogens as well as oxygen–silver interactions. Hydrogen bonding occurs *via* the oxygen that faces away from its ASU and the nearest diagonal hydrogens from adjacent molecules (Fig. 9a). The sum of van der Waals radii for hydrogen–oxygen is ($R_H + R_O$ = 2.72 Å), and **VII** has distances of d(H⋯O) = 2.380(18) Å, which indicates a strong molecular orbital interaction that significantly influences the packing along the *b*-axis. Silver–oxygen interactions occur along the *c*-axis to guide packing along this direction. The nitrate molecules are angled such that two of the oxygens interact with silver(I) metal centres, Fig. 9b. The distance between the oxygen and silver d(O⋯Ag) = 2.766(3) Å, which is significantly less than the sum of the van de Waals radii for oxygen–silver interactions ($R_O + R_{Ag}$ = 3.24 Å), is highly suggestive of molecular orbital interactions. The large difference in distance demonstrates a strong influence on packing in this direction.

A survey of the Cambridge Structural Database[32] found 775 structures containing a silver(I) ion with two pyridyl ligands
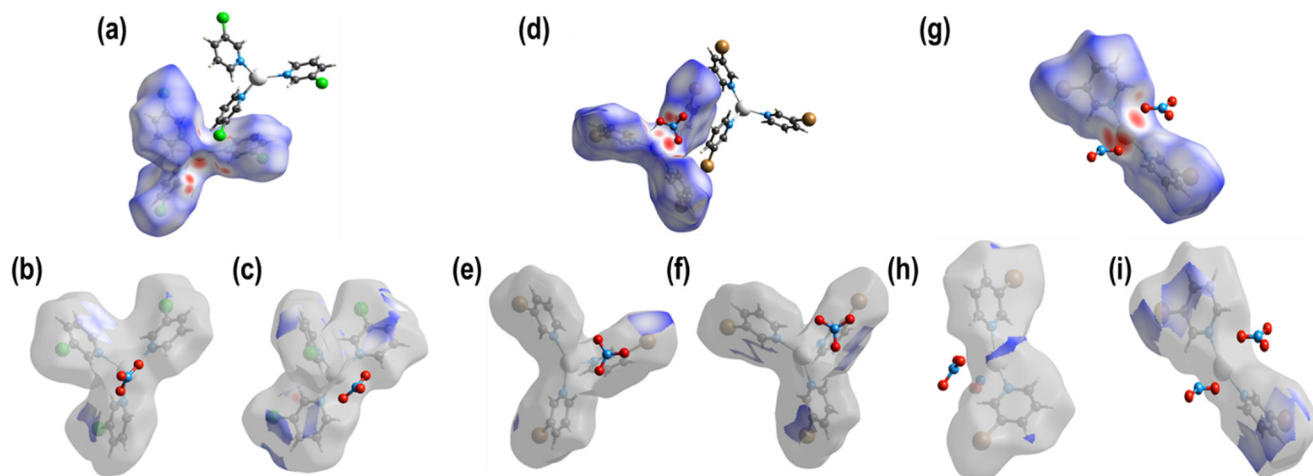

Fig. 10 Hirshfeld surfaces of **V**: (a) HS coverage (d_{norm}), (b) C⋯C contacts, and (c) C⋯H contacts [blue and white patches]; **VI**: (d) HS coverage (d_{norm}), (e) Br⋯Br contacts, and (f) C⋯C contacts; and **VII**: (g) HS coverage (d_{norm}), (h) H⋯Ag contacts, and (i) Br⋯C contacts.

and 2-coordinate geometry. The average Ag–N bond distance for these is 2.17(6) Å, which compares well to the values reported for compounds **I, II, III** and **VII**. Most adopt an almost linear geometry with an average N–Ag–N bond angle of 171(10)°. We found that **VII** adopted a bent geometry, which is well represented in the structures reported in the CSD, 233 of which have a bond angle less than 170°.

Most of the 65 propeller (3-coordinate) structures surveyed adopt near trigonal planar coordination geometry. Of the remainder, there is a cluster of twelve structures that adopt a similar geometry to the 3-coordinate structures reported here, with Ag–N bond distances of 2.29(8) Å and N–Ag–N bond angles of 105(3), 115(5) and 137(7)°. These values compare well with those reported here for **IV, V** and **VI**.

Hirshfeld surface (HS) analysis

Hirshfeld surfaces (HSs) were calculated for compounds **V, VI** and **VII** to provide a visualisation of relevant non-covalent interactions present in the halogenated complexes.
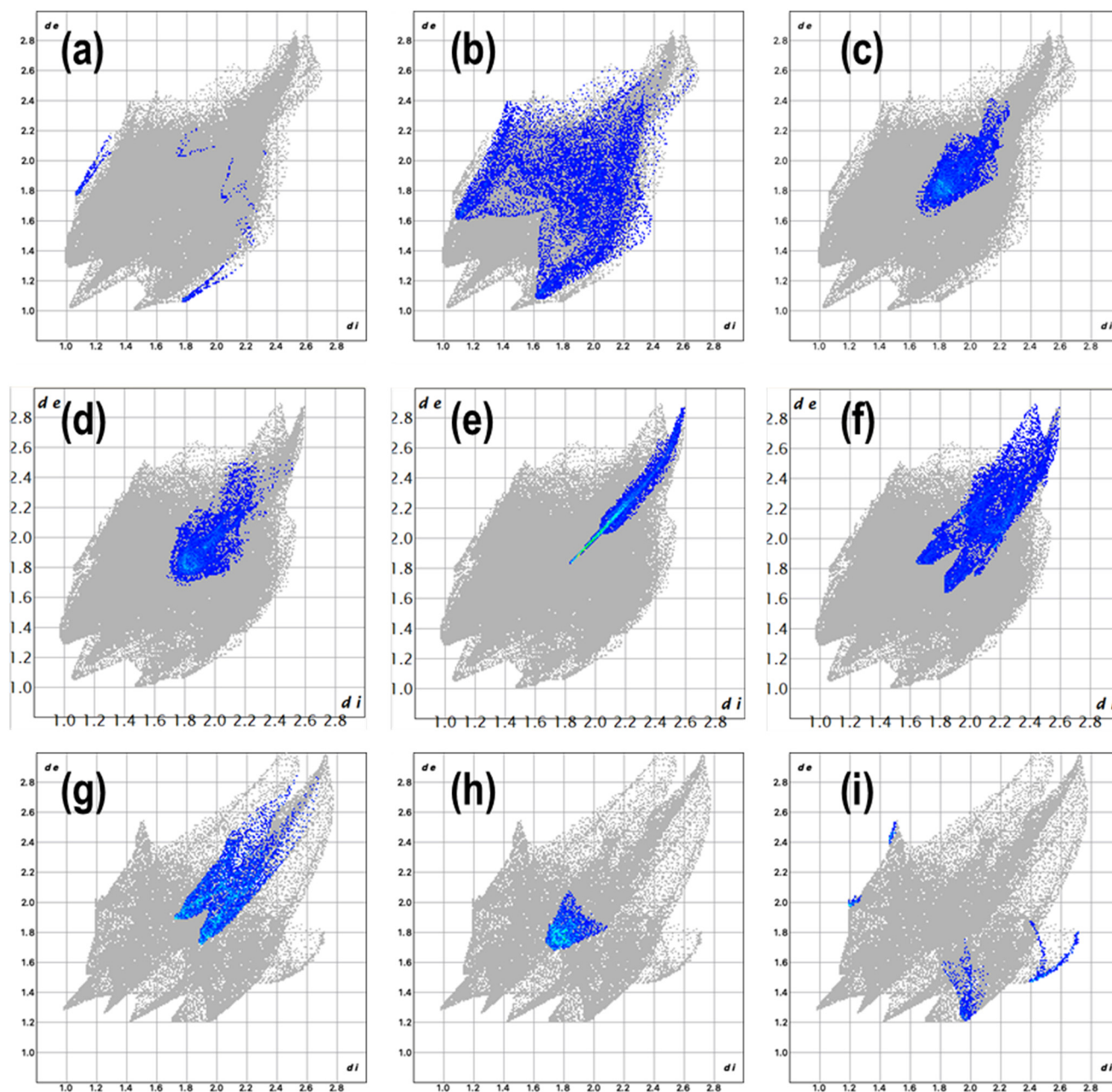

Fig. 11 Fingerprint plots for **V–VII**, translated and filtered by element contacts. **V**: (a) Ag⋯H/H⋯Ag contacts (0.5% of HS area); (b) C⋯H/H⋯C contacts (10.8%); and (c) C⋯C/C⋯C contacts (5.5%). The grey area represents the entire surface. **VI**: (d) Br⋯C/C⋯Br contacts (9.2%); (e) Br⋯Br contacts (5.7% of HS area); and (f) C⋯C contacts (5.9%). **VII**: (g) Br⋯C/C⋯Br contacts (13.5% of HS area); (h) C⋯C/C⋯C contacts (5.3%); and (i) Ag⋯H/H⋯Ag contacts (2.0%).

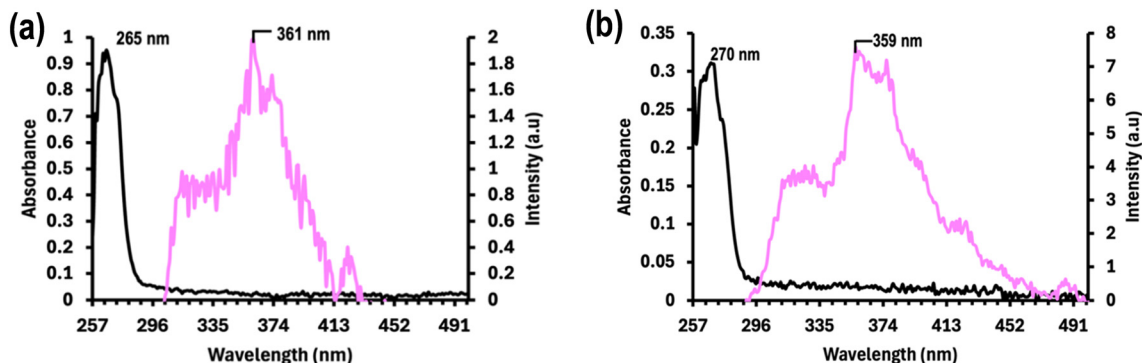**Fig. 12** Absorption (black) and emission (purple) spectra of (a) **I** [Ag(2,3-Lut)$_2$(NO$_3$)] and (b) **VI** [Ag(3-Brpy)$_3$(NO$_3$)].

Fig. 10 shows the mapping of the HS using the parameters d_{norm}, d_i and d_e. Intermolecular contacts were further investigated using translated fingerprint plots (FP), providing 2D representations of the data (Fig. 11).

In **V**, the notable feature is the $\pi \cdots \pi$ interaction suggested by the Cg1$\cdots$Cg2 distance of 3.585(16) Å. HS analysis supports this being a weak molecular orbital interaction, as shown in Fig. 10b, with highlighted blue and white patches. Carbon–hydrogen interactions are also observed to have a notable influence on crystal packing (as shown in Fig. 10c). As suggested by the crystal structure analysis, chlorine–chlorine interactions are minimal. To quantify the contribution of these interactions to crystal packing, fingerprint plots were analysed. The $\pi \cdots \pi$ interaction forms a conical shape at $(d_e + d_i) = 3.6$ Å (Fig. 11c), contributing 5.5% to the total Hirshfeld surface area. In comparison, carbon–hydrogen interactions, represented by a plier-shaped feature depicted in Fig. 11b at $(d_e + d_i) = 3.2$ Å, contribute a more substantial 10.8% to the surface area. Silver–hydrogen interactions are minimal, accounting for only 0.5% of the surface area, Fig. 11a.

Hirshfeld surface analysis confirms the presence of Br$\cdots$Br contacts (Fig. 10e) and $\pi \cdots \pi$ interactions (Fig. 10f) in **VI**. The fingerprint plots indicate that the main contribution

is from the bromine–carbon interactions at 9.2%, while bromine–bromine interactions (5.7%) and carbon–carbon interactions from the π stacking (5.9%) make almost equal contributions (Fig. 11d–f).

The Hirshfeld surface of **VII** is shown in Fig. 10g, which confirms the presence of silver–oxygen interactions, as well as hydrogen–silver interactions (Fig. 10h) and bromine–carbon interactions (Fig. 10i). The fingerprint plots show that the main contribution to the surface area comes from the bromine–carbon interactions at 13.5%. This is shown as two sharp peaks with $(d_e + d_i) = 3.7$ Å in Fig. 11g and corresponds well to the distance from the bromine to an aromatic centroid measured in the crystal structure as 3.688(2) Å. The carbon–carbon interactions (primarily in the weak π stacking) are illustrated in Fig. 11h, where the conical shape with $(d_e + d_i) = 3.4$ Å contributes 5.3% towards the HS. The silver–hydrogen interactions observed in the crystal structure account for 2.0% of the HS (Fig. 11i).

UV-vis and emission spectra

Spectroscopic analysis was performed on complex **I–VII** by means of ultraviolet-visible (UV-vis) spectroscopy, emission
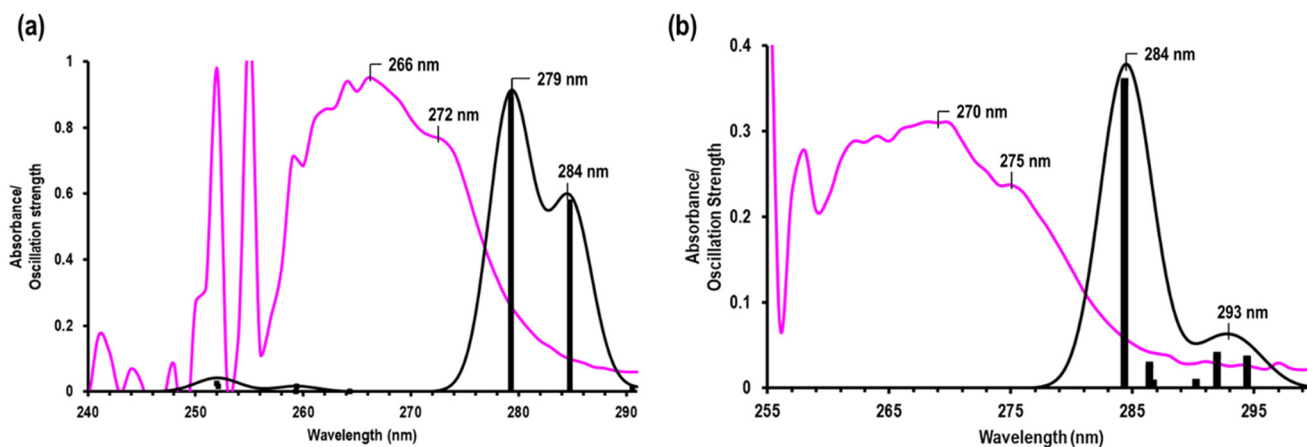

Fig. 13 B3LYP TDDFT-computed oscillators (bars) using MeCN and DMSO as solvents, overlaid with Gaussian broadening curves (black) and the experimental UV-visible spectra (magenta) of Ag(2,3-Lut)$_2$(NO$_3$) in MeCN (a) and Ag(3-Brpy)$_3$(NO$_3$) in DMSO (b).

Table 1 DFT-calculated absorbance maximum wavelengths ($\lambda_{Abs.\ max}$) and maximum wavelengths (λ_{max}) compared with experimental wavelengths in nm

Complex	DFT-calculated		Experimental data	
	$\lambda_{Abs.\ max}$ (nm)	λ_{max} (nm)	$\lambda_{Abs.\ max}$ (nm)	λ_{max} (nm)
I	284	292	266	272
VI	279	284	270	275

spectroscopy (ES), and Fourier-transform infrared (FTIR) spectroscopy. FTIR analysis confirmed the presence of expected functional groups, such as C–N ($\approx$1300 cm^{-1}), aromatic C–H ($\approx$3100 cm^{-1}), and halogenated peaks (650–750 cm^{-1}). Each series exhibited comparable graphical characteristics, allowing for the selection of a representative complex from each series for further analysis. Complexes **I** and **VI** were chosen as representative samples of the lutidine

and halopyridine series and are described here. Data for the remaining complexes can be found in the SI. UV-vis analysis of these complexes revealed maximum absorption peaks at $\lambda_{Abs.\ max}$ = 265 nm for **I** and $\lambda_{Abs.\ max}$ = 270 nm for **VI** (Fig. 12). Peaks in this wavelength range indicate metal-to-ligand-charge-transfer (MLCT) transitions from the metal orbitals to low-lying π^* orbitals on the ligands.[33] Similar phenomena have been reported for coordination complexes with π-acceptor ligands.[34–36]

Emission spectra were also collected, showing emission maxima at $\lambda_{Em.\ max}$ = 361 nm for **I** and $\lambda_{Em.\ max}$ = 359 nm for **VI** (Fig. 12). The difference between the absorption and emission maxima, known as the Stokes shift, was calculated to be 96 nm for **I** and 89 nm for **VI**, indicating a significant shift in energy between the excitation and emission processes. This large Stokes shift reflects energy dissipation during excited-state relaxation, which further supports the
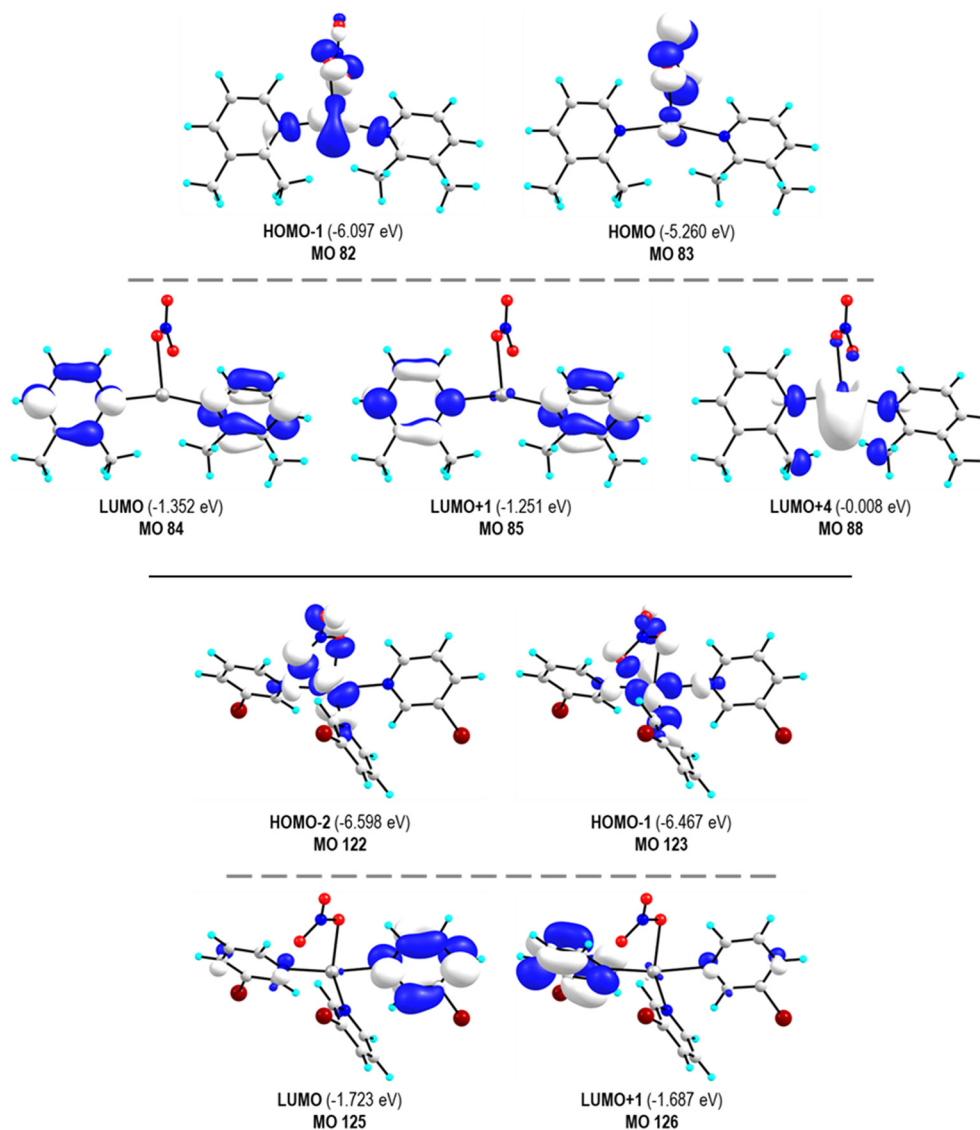

Fig. 14 Selected MOs for I and VI, with energies (in eV) indicated in brackets. The orbital plots were generated using a contour value of 0.05 e Å^{-3}. Atoms are colour-coded as follows: Ag (grey), Br (brown), C (white), H (cyan), N (blue), and O (red).
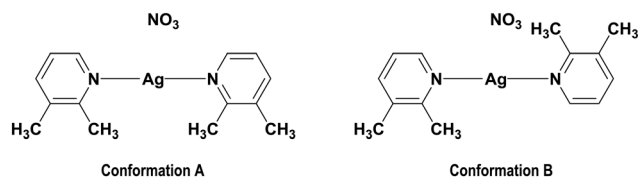
Fig. 15 Two conformations (A and B) of 2,3-Lut ligands in complex I.

MLCT nature of the transitions and highlights the potential fluorescent properties of these complexes. A weak shoulder band is observed around 315 nm in the emission spectra of **I** and **VI** (Fig. 12). This feature arises from intraligand charge transfer ($\pi \rightarrow \pi^*$) transitions, which are slightly perturbed by coordination with the silver(I) center. Such ligand-dominated emissions have been reported for a variety of silver(I) complexes, where they often appear as higher-energy shoulders separate from the main MLCT emission band.[37–39]

Computational results

UV-visible spectroscopy and TDDFT calculations. Compounds **I** and **VI** were selected for computational studies as representative samples of the lutidine and halopyridyl series, as well as of the linear and propeller geometries. The simulated UV-visible spectra of compounds **I** and **VI** were obtained using time-dependent density-functional theory (TDDFT) at the B3LYP/cc-pVDZ level of theory (cc-PVDZ-PP for Ag). The experimental spectra display λ_{max} bands above 260 nm (Fig. 13), consistent with metal-to-ligand charge transfer (MLCT) transitions, and the calculated spectra show good agreement with these observations. The largest deviation between the experimental and theoretical λ_{max} values is 17 nm (Table 1). The calculations thus provide strong support for the experimental assignments.

To probe the electronic nature of the main absorptions, the molecular orbitals (MOs) contributing to the $\lambda_{Abs.\ max}$ and λ_{max} transitions were analysed (Table S5 and Fig. 14). The dominant excitations arise from the metal-centred HOMO and HOMO−1 orbitals (Ag d-orbitals) to the ligand-centred LUMO and LUMO+1 orbitals (π^*). These results confirm the MLCT character of the absorptions, specifically involving electron density transfer from the Ag-d to the ligand-π^* orbitals, in line with expectations for Ag(I)-pyridyl coordination complexes.

Potential energy surface (PES) scan. Compound **I** was selected to explore the conformational landscape of the $[Ag(2,3-Lut)_2]$ moiety, which can adopt two distinct conformations (A and B, Fig. 15).

A potential energy surface (PES) scan was performed by varying dihedral angle D1 (O1–Ag1–N1–C2) in 30 steps of $10°$ increments. Scanning to $240°$ was sufficient to capture a unique conformational space, as further rotation reproduces equivalent geometries by symmetry. The resulting energy profile (Fig. 16) was referenced to the global minimum (set to 0.00 kcal mol^{-1}) and revealed four minima at $0°$, $50°$, $130°$, and $180°$, separated by barriers of approximately 1.5 and 2.5 kcal mol^{-1}. These correspond to the *syn* and *anti*-geometries of the pyridyl rings. Fig. 16 further shows that the experimental crystal structure aligns with the lowest-energy conformer, validating the computational model.

The small energy differences among conformers (≤ 2.5 kcal mol^{-1}) indicate ligand flexibility. Such flexibility, although observed here for a discrete Ag–N complex, could be beneficial in the design of functionalized MOFs (FL-MOFs), where adaptable ligands enable reversible framework transformations during guest accommodation. This study highlights the potential of Ag–N coordination to support ligand flexibility, an important consideration for future FL-MOF design.
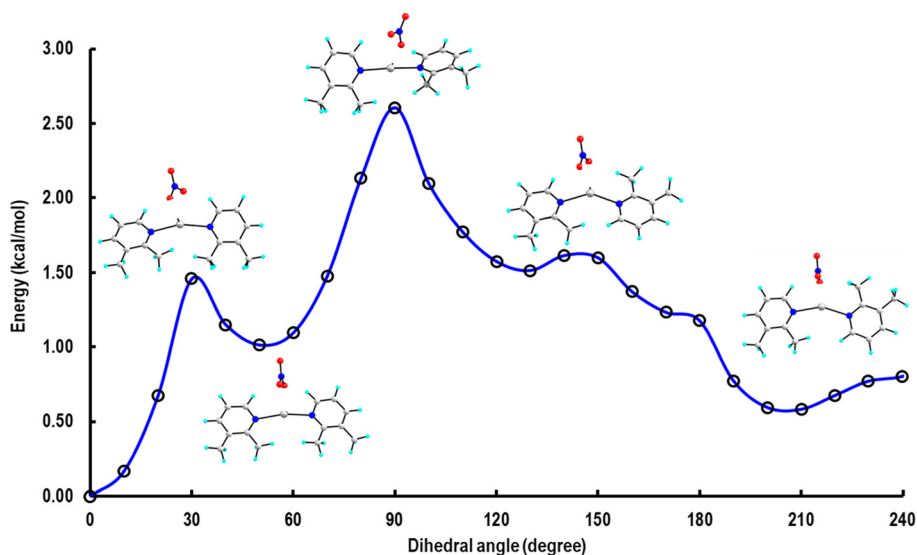

Fig. 16 Potential energy surface scan for the dihedral angle D1 (O1–Ag1–N1–C2).

Conclusions

In this study, we describe two series of silver(I)-pyridyl complexes. Four lutidine derivatives afforded structures of $[Ag(2,3\text{-}Lut)_2(NO_3)]$ (**I**), $[Ag(2,6\text{-}Lut)_2(NO_3)]$ (**II**), $[Ag(3,4\text{-}Lut)_2(NO_3)(H_2O)]$ (**III**), and $[Ag(3,5\text{-}Lut)_3(NO_3)]$ (**IV**), while halogenated pyridyl complexes are represented by $[Ag(3\text{-}Clpy)_3(NO_3)]$ (**V**), $[Ag(3\text{-}Brpy)_3(NO_3)]$ (**VI**), and $[Ag(3\text{-}Brpy)_2(NO_3)]$ (**VII**).

Three-coordinate, propeller-like geometry was observed in **IV**, **V** and **VI**, while the two-coordinate geometry was linear for **I**, **II** and **III** but bent for **VII**. The halogenated pyridyl complexes (**V**–**VII**) favoured π–π stacking between aromatic rings (π-systems), with opposite-facing halogens on adjacent rings. This stacking likely results from steric and electrostatic effects. Large atomic radii of halogens may lead to steric strain, while electrostatic interactions between the halogens and aromatic rings guide positioning. A selective Hirshfeld surface analysis of complex **VII** revealed a noteworthy aromatic ring-bromine interaction.

Other NCIs observed in the halogenated complexes included Ag···H (agostic) interactions, electrostatic interactions between the silver centre and nitrate oxygen $[Ag^+\cdots O_2\text{-}N\text{-}O\cdots Ag^+]$ in **V**, Ag···H agostic and Br···Br interactions in **VI**, and weak hydrogen bonding $[O\cdots H\text{-}C]$ along with Ag···O interactions in **VII**.

The lutidine complexes (**I**–**IV**) displayed different types of π-interactions. Although **I** lacked π–π interactions and was primarily stabilised by oxygen-involved interactions, complexes **II**–**IV** exhibited aromatic-hydrogen (Cg···H) interactions involving methyl groups. The electron-donating nature of the methyl groups enhanced the electron density in the ring, which attracted the slightly positive hydrogen atoms towards the electron-rich aromatic ring, facilitating Cg···H interactions rather than π–π interactions. Additional NCIs included Ag···O and C–H···O interactions in **I**, C–H···O interactions in **II**, weak hydrogen bonding (H···O), C···H interactions, Ag···O interactions in **III**, and Ag···H agostic interactions in **IV**.

Ultraviolet-visible (UV-vis) spectroscopy and emission spectroscopy (ES) revealed fluorescence properties for all complexes, with absorbance peaks around 260–280 nm and emissions in the range of 360–375 nm. The observed excitations are consistent with metal-to-ligand charge transfer (MLCT) from the Ag(I) d-orbitals to the ligand π^* orbitals. The TDDFT calculations correlated with the experimental UV-vis data. Molecular orbital (MO) analysis indicated that the transitions were primarily from the metal-based HOMO and HOMO−1 to the ligand-based LUMO and LUMO+1, supporting the MLCT character.

A potential energy surface (PES) scan of complex **I** revealed low energy barriers (1.5 kcal mol^{-1} and 2.5 kcal mol^{-1}) between the *syn-* and *anti-*geometries of the 2,3-Lut ligands, indicating a high degree of flexibility with minimal energy cost. This flexibility could be advantageous for the design of MOFs that require conformational adaptability during guest accommodation.

This investigation gives an overview of how various substituents affect overall crystal stability and packing arrangements and provides a foundation for the further exploration of silver(I) complexes in design and other applications.

Author contributions

ELG: investigation, analysis, writing – original draft; TKT: conceptualisation, supervision, analysis, writing – review & editing; SAB: conceptualisation, supervision, writing – review & editing.

Conflicts of interest

There are no conflicts to declare.

Data availability

The data supporting this article have been included as part of the supplementary information (SI).

Supplementary information: this includes crystallographic details, diagrams and tables of non-covalent interactions, computational details, FTIR and UV-vis and emission spectra, and PXRD. See DOI: https://doi.org/10.1039/d5ce00879d.

CCDC 2486323–2486329 contain the supplementary crystallographic data for this paper.[40a–g]

Acknowledgements

References

1 J. Jimenez, I. Chakraborty, A. M. Del Cid and P. K. Mascharak, Five-and six-coordinated silver (I) complexes derived from 2, 6-(pyridyl) iminodiadamantanes: sustained release of bioactive silver toward bacterial eradication, *Inorg. Chem.*, 2017, **56**, 4784–4787.

2 A. Altay, S. Caglar, B. Caglar and Z. S. Sahin, Novel Silver(I) Complexes Bearing Mefenamic Acid and Pyridine Derivatives: Synthesis, Chemical Characterization and in Vitro Anticancer Evaluation, *Inorg. Chim. Acta*, 2019, **493**, 61–71.

3 R. A. Haque, S. Budagumpi, H. Zetty Zulikha, N. Hasanudin, M. B. Khadeer Ahamed and A. M. S. Abdul Majid, Silver(I)-N-Heterocyclic Carbene Complexes of Nitrile-Functionalized Imidazol-2-Ylidene Ligands as Anticancer Agents, *Inorg. Chem. Commun.*, 2014, **44**, 128–133.

4 U. Kalinowska-Lis, A. Felczak, L. Chęcińska, I. Szabłowska-Gadomska, E. Patyna, M. Małecki, K. Lisowska and J. Ochocki, Antibacterial Activity and Cytotoxicity of Silver(I)

Complexes of Pyridine and (Benz)Imidazole Derivatives. X-Ray Crystal Structure of [Ag(2,6-Di(CH2OH)Py)2]NO3, *Molecules*, 2016, **21**, 87.

5 R.-S. Wand, J. Feng, Y.-Z. Lei, D.-M. Chen and M.-L. Lian, New 3D Supramolecular Ag(I) Coordination Polymer Crystal Containing 2-Quinaldic Acid Radical Biological Ligand: Crystal Structure and Anticancer Activity, *Cryst. Res. Technol.*, 2018, **53**, 1800065.

6 X.-P. Wang, T.-P. Hu and D. Sun, Luminescent silver(I) coordination architectures containing 2-aminopyrimidyl ligands, *CrystEngComm*, 2015, **17**, 3393–3417.

7 C.-C. Chen, Y. Cai, L.-F. Wang, Y.-D. Wu, H.-J. Yin, J.-R. Zhou, C.-L. Ni and W. Liu, Three Silver(I) Coordination Polymers Based on Pyridyl Ligands and Auxiliary Carboxylic Ligands: Luminescence and Efficient Sensing Properties, *Inorg. Chem.*, 2021, **60**, 5463–5473.

8 T. Zhang, H.-Q. Huang, H.-X. Mei, D.-F. Wang, X.-X. Wang, R.-B. Huang and L.-S. Zheng, New Silver(I) Coordination Polymers Constructed from Pyrazine Derivatives and Aromatic Carboxylic Acids: Syntheses, Structures and Photoluminescence, *J. Mol. Struct.*, 2015, **1100**, 237–244.

9 S. Mondal, R. Sahoo, J. Behera and M. C. Das, Advances on silver-based MOFs and/or CPs and their composites: Synthesis strategies and applications, *Coord. Chem. Rev.*, 2024, **514**, 215924.

10 V. W.-W. Yam and K. K.-W. Lo, Luminescent polynuclear d10 metal complexes, *Chem. Soc. Rev.*, 1999, **28**, 323–334.

11 K. E. Riley and P. Hobza, Noncovalent Interactions in Biochemistry, *Wiley Interdiscip. Rev.: Comput. Mol. Sci.*, 2011, **1**, 3–17.

12 J. Chen, Q. Peng, X. Peng, H. Zhang and H. Zeng, Probing and Manipulating Noncovalent Interactions in Functional Polymeric Systems, *Chem. Rev.*, 2022, **122**, 14594–14678.

13 P. Metrangolo, H. Neukirch, T. Pilati and G. Resnati, *Acc. Chem. Res.*, 2005, **38**(5), 386–395.

14 P. Scilabra, G. Terraneo and G. Resnati, *Acc. Chem. Res.*, 2019, **52**(5), 1313–1324.

15 P. Politzer, J. S. Murray, T. Clark and G. Resnati, *Phys. Chem. Chem. Phys.*, 2017, **19**, 32166–32178.

16 T. K. Theunissen, C. Esterhuysen and S. A. Bourne, Dominant Metal-NCIs Stabilizing Crystal Packing in Silver(I)-Pyridyl Compounds: Insights from Crystallographic and Computational Studies, *Cryst. Growth Des.*, 2024, **24**, 9254–9265.

17 *Program SAINT*, Bruker AXS Inc, Madison, Wisconsin, USA, 2006.

18 G. M. Sheldrick, *SADABS: Program for Area Detector Absorption Correction*, University of Gottingen, Germany, 1996.

19 *XPREP: Data Preparation & Reciprocal Space Group Exploration, Version 5.1*, Bruker AXS Inc, Madison, Wisconsin, USA, 1997.

20 O. V. Dolomanov, L. J. Bourhis, R. J. Gildea, J. A. K. Howard and H. Puschmann, OLEX2: a complete structure solution, refinement and analysis program, *J. Appl. Crystallogr.*, 2009, **42**, 339–341.

21 G. M. Sheldrick, A short history of SHELX, *Acta Crystallogr., Sect. A: Found. Crystallogr.*, 2008, **64**, 112–122.

22 C. F. Macrae, I. Sovago, S. J. Cottrell, P. T. A. Galek, P. McCabe, E. Pidcock, M. Platings, G. P. Shields, J. S. Stevens, M. Towler and P. A. Wood, Mercury 4.0: From Visualization to Analysis,Design and Prediction, *J. Appl. Crystallogr.*, 2020, **53**, 226–235.

23 M. J. Frisch, G. W. Trucks, H. B. Schlegel, G. E. Scuseria, M. A. Robb, J. R. Cheeseman, G. Scalmani, V. Barone, G. A. Petersson, H. Nakatsuji, X. Li, M. Caricato, A. V. Marenich, J. Bloino, B. G. Janesko, R. Gomperts, B. Mennucci, H. P. Hratchian, J. V. Ortiz, A. F. Izmaylov, J. L. Sonnenberg, D. Williams-Young, F. Ding, F. Lipparini, F. Egidi, J. Goings, B. Peng, A. Petrone, T. Henderson, D. Ranasinghe, V. G. Zakrzewski, J. Gao, N. Rega, G. Zheng, W. Liang, M. Hada, M. Ehara, K. Toyota, R. Fukuda, J. Hasegawa, M. Ishida, T. Nakajima, Y. Honda, O. Kitao, H. Nakai, T. Vreven, K. Throssell, J. A. Montgomery Jr , J. E. Peralta, F. Ogliaro, M. J. Bearpark, J. J. Heyd, E. N. Brothers, K. N. Kudin, V. N. Staroverov, T. A. Keith, R. Kobayashi, J. Normand, K. Raghavachari, A. P. Rendell, J. C. Burant, S. S. Iyengar, J. Tomasi, M. Cossi, J. M. Millam, M. Klene, C. Adamo, R. Cammi, J. W. Ochterski, R. L. Martin, K. Morokuma, O. Farkas, J. B. Foresman and D. J. Fox, *Gaussian 16, Revision C.01*, Gaussian, Inc., Wallingford CT, 2016.

24 A. D. Becke, Density-Functional Exchange-Energy Approximation with Correct Asymptotic Behavior, *Phys. Rev. A: At., Mol., Opt. Phys.*, 1988, **38**, 3098–3100.

25 C. Lee, W. Yang and R. G. Parr, Development of the Colle-Salvetti Correlation-Energy Formula into a Functional of the Electron Density, *Phys. Rev. B: Condens. Matter Mater. Phys.*, 1988, **37**, 785–789.

26 T. H. Dunning, Gaussian Basis Sets for Use in Correlated Molecular Calculations. I. The Atoms Boron through Neon and Hydrogen, *J. Chem. Phys.*, 1989, **90**, 1007–1023.

27 D. Figgen, G. Rauhut, M. Dolg and H. Stoll, *Chem. Phys.*, 2005, **311**, 227–244.

28 S. Grimme, J. Antony, S. Ehrlich and H. Krieg, A Consistent and Accurate Ab Initio Parametrization of Density Functional Dispersion Correction (DFT-D) for the 94 Elements H-Pu, *J. Chem. Phys.*, 2010, **132**, 154104.

29 S. Grimme, S. Ehrlich and L. Goerigk, Effect of the Damping Function in Dispersion Corrected Density Functional Theory, *J. Comput. Chem.*, 2011, **32**, 1456–1465.

30 Chemcraft, *Chemcraft – graphical software for visualization of quantum chemistry computations*, https://www.chemcraftprog.com/.

31 P. R. Spackman, M. J. Turner, J. J. McKinnon, S. K. Wolff, D. J. Grimwood, D. Jayatilaka and M. A. Spackman, *J. Appl. Crystallogr.*, 2021, **54**, 1006–1011.

32 C. R. Groom, I. J. Bruno, M. P. Lightfoot and S. C. Ward, The Cambridge structural database, *Acta Crystallogr., Sect. B: Struct. Sci., Cryst. Eng. Mater.*, 2016, **72**, 171–179.

33 A. K. Brisdon, UV-Visible Spectroscopy, in *Inorganic Spectroscopic Methods*, Oxford UP, Oxford, 1998, pp. 70–73.

34 G. Mehlana, S. A. Bourne and G. Ramon, A new class of thermos- and solvatochromic metal-organic frameworks

based on 4-(pyridine-4-yl)benzoic acid, *Dalton Trans.*, 2012, **41**, 4224–4231.

35 C. N. Dzesse T., E. N. Nfor and S. A. Bourne, Vapor sorption and solvatochromism in a metal-organic framework of an asymmetric pyridylcarboxylate, *Cryst. Growth Des.*, 2018, **18**, 416–423.

36 C. A. Ndamyabera, S. C. Zacharias, C. L. Oliver and S. A. Bourne, Solvatochromism and selective sorption of volatile organic solvents in pyridylbenzoate metal-organic frameworks, *Chemistry*, 2019, **1**, 111–125.

37 J. F. Endicott, H. B. Schlegel, Md. J. Uddin and D. S. Seniveratne, MLCT excited states and charge delocalization in some ruthenium-ammine-polypyridyl complexes, *Coord. Chem. Rev.*, 2002, **229**, 95–106.

38 K. Matsumoto, T. Shindo, N. Mukasa, T. Tsukuda and T. Tsubomura, Luminescent mononuclear Ag(I)-bis(diphosphine) complexes: Correlation between the photophysics and the structures of mononuclear Ag(I)-bis(diphosphine) complexes, *Inorg. Chem.*, 2010, **49**, 805–814.

39 S. Kumar, D. Mondal and M. S. Balakrishna, Diverse architectures and luminescence properties of group 11 complexes containing pyrimidine-based phosphine, N-((diphenylphosphine)methyl)pyrimidin-2-amine, *ACS Omega*, 2018, **12**, 16601–16614.

40 (*a*) CCDC 2486323: Experimental Crystal Structure Determination, 2025, DOI: 10.5517/ccdc.csd.cc2pg6zc; (*b*) CCDC 2486324: Experimental Crystal Structure Determination, 2025, DOI: 10.5517/ccdc.csd.cc2pg70f; (*c*) CCDC 2486325: Experimental Crystal Structure Determination, 2025, DOI: 10.5517/ccdc.csd.cc2pg71g; (*d*) CCDC 2486326: Experimental Crystal Structure Determination, 2025, DOI: 10.5517/ccdc.csd.cc2pg72h; (*e*) CCDC 2486327: Experimental Crystal Structure Determination, 2025, DOI: 10.5517/ccdc.csd.cc2pg73j; (*f*) CCDC 2486328: Experimental Crystal Structure Determination, 2025, DOI: 10.5517/ccdc.csd.cc2pg74k; (*g*) CCDC 2486329: Experimental Crystal Structure Determination, 2025, DOI: 10.5517/ccdc.csd.cc2pg75l.